Spatiotemporal Heterogeneity of *b* Values Revealed by a Data-Driven Approach for June 17, 2019 *M*S 6.0, Changning Sichuan, China Earthquake Sequence

Changsheng Jiang[1*], Libo Han[1], Feng Long[2], Guijuan Lai[1], Fengling Yin[1], Jinmeng Bi[3], Zhengya Si[4]

[1] Institute of Geophysics, China Earthquake Administration, Beijing 100081, China

[2] Sichuan Earthquake Agency, Chengdu 610041, China

[3] Tianjin Earthquake Agency, Tianjin 300201, China

[4] Beijing Earthquake Agency, Beijing 100080, China

Correspondence to: Changsheng Jiang (jiangcs@cea-igp.ac.cn)

Abstract. The spatiotemporal heterogeneity of *b* values has great potential for understanding the seismogenic process and assessing the seismic hazard. However, there is still much controversy about whether it exists or not, and an important reason is that the choice of subjective parameters has eroded the foundations of many researches. To overcome this problem, we used a recent developed non-parametric method based on the data-driven concept to calculate *b* values. The major steps of this method include: 1) perform a large number of Voronoi tessellation, Bayesian information criterion (BIC) value calculation and selection of the optimal models for the study area, and 2) use the ensemble median (Q_2) and median absolute deviation (MAD) value to represent the final *b* value and its uncertainty. We investigated spatiotemporal variations of *b* values before and after the 2019 Changning *M*S 6.0 earthquake in Sichuan Basin, China. The results reveal a spatial volume with low pre-mainshock *b* values near the mainshock source region, and its size corresponds roughly with the rupture area of the mainshock. The anomalously high pre-mainshock *b* values distributed in the NW direction of the epicenter was interpreted to be related with fluid invasion. The decreases of *b* values during the aftershock sequence along with the occurrences of several strong aftershocks imply that *b* values could be an indicator of stress state. In addition, we found that although the distribution characteristics of *b* values obtained from different way of investigating are qualitatively consistent, they differ significantly in terms of their specific values, suggesting that the best way to study the heterogeneous pattern of *b* values is in the joint dimension of space-time rather than alone in time and space. Overall, our study emphasizes the importance of *b* value studies on assessing the earthquake hazards.

Keywords *b* value; data-driven; spatiotemporal heterogeneity; Ogata-Katsura 1993 model; Voronoi tessellation

Introduction

The Gutenberg-Richter b value describes the corresponding frequency-magnitude distribution (FMD) characteristics by reflecting the relative proportion of the frequency of large and small earthquakes within a given space-time range. It is considered to be related to the stress conditions in the Earth's crust (e.g., Wyss, 1973; Urbancic et al., 1992; Mori and Abercrombie, 1997; Toda et al., 1998), complexity of the fault trace (Stirling et al., 1996), and the extent of creep (Amelung and King, 1997) and other factors. Experimental studies in the laboratory have shown that a weak and less resistant environment under stress would produce a high b value, while materials that are more compact and more resistant under pressure do not fail, which leads to a reasonable low b value (Aktar et al., 2004). In the case where the material and structure are clarified, decreasing b value is considered to be related to increasing stress (Scholz, 1968) or pore pressure diffusion (Hainzl and Fischer, 2002; Lei and Satoh, 2007). For the above reasons, b value has been widely concerned in seismogenic environment analysis and seismic hazard research.

Spatial and temporal heterogeneity is an important topic in b value research, especially under the assumption that the local b values are inversely dependent on the applied shear stress, and that low b values ($b < 0.7$) can reflect the existence of locked faults or asperities. Therefore, the spatial and temporal heterogeneity of b values is considered as an important clue for forecasting the location and size of potential large earthquakes (Wiemer and Wyss, 1997; Schorlemmer and Wiemer, 2005; Murru et al., 2007). Using the spatial heterogeneity of b value to identify possible asperities is performed in some cases, such as the San Jacinto-Elsinore fault system in southern California (Wyss et al., 2000), the Parkfield segment of the San Andreas fault (Wiemer and Wyss, 1997), and the case study of the 2014 Parkfield M 6.0 earthquake (Schorlemmer and Wiemer, 2005).

A model named Asperity Likelihood Model (ALM) based on the above assumptions has been developed and used to forecast future earthquakes (Wiemer and Schorlemmer, 2007; Gulia et al., 2010). The research on the temporal heterogeneity of b values mainly includes using b value time variation of early aftershock sequence and the constructed system of foreshock traffic light system (FTLS) to evaluate the risk of subsequent larger aftershocks (Gulia and Wiemer, 2019).

However, some research results show that the apparent variability of b values is not significant in some cases (Del Pezzo et al., 2003). For example, Amorèse et al. (2010) systematically examined the variation

61 of b values in Southern California to the depth of the crust, and found that the hypothesis was not

62 statistically significant. By using a data-driven approach, Kamer and Hiemer (2015) shows that the

63 spatial b values in most locations in California are distributed within a very limited range (0.94 ± 0.04–

64 1.15 ± 0.06), and the previously reported spatial b value variation is overestimated and mainly due to the

65 subjective choice of parameters. Besides, the spatial and temporal heterogeneity of b values is also

66 considered to be due to the subjective arbitrariness of the calculation rules and the lack of statistical

67 robustness (Kagan 1999).

68 Based on the above viewpoints, the calculation reliability for researches on the spatiotemporal

69 heterogeneity of b values still needs to be solved, and the relationship between the spatiotemporal

70 variation process of b values and the occurrence of strong earthquakes need to be investigated for more

71 earthquake cases. In this study, we will utilize data-driven based b values calculation methods that have

72 been developed in recent years (Kamer and Hiemer, 2015; Nandan et al., 2017; Si and Jiang, 2019) for

73 case studies of the 2019 Changning M_S 6.0 earthquake in Sichuan, China.

74 **Method**

75 In the traditional calculation of the Guttenberg-Richter magnitude-frequency b value, a fixed number of

76 earthquakes (Hutton et al., 2010; Ogata, 2011) or a fixed minimum and maximum selection radius

77 (Woessner and Wiemer, 2005) are generally used to select data and the maximum likelihood estimation

78 is used to obtain b values. Because such calculations have strong subjectivity in calculating rules, it has

79 caused widespread controversy. The data-driven approaches to seismicity parameter calculation have

80 been gradually developed in recent years (Sambridge et al., 2013; Kamer and Hiemer, 2015; Nandan et

81 al., 2017; Si and Jiang, 2019), by using the Voronoi tessellation to create a large number of spatially

82 random grids and covering the possibility of segmentation of spatial regions, relying on the Bayesian

83 information criterion (BIC) to select a part of the optimal models with the smallest BIC value, and

84 representing the final result of seismic activity parameters through the ensemble median value. Because

85 the data-driven approach uses an automatic parametric calculation, it provides a possibility for solving

86 the subjective problem of earthquake data selection.

87 Among those data-driven approaches, Si and Jiang (2019) developed a method using continuous

88 distribution function (hereafter referred to as OK1993 model) given by Ogata and Katsura (1993), which

89   has the advantage of simultaneously determining the minimum magnitude of completeness and obtaining

90   *b* values. In this paper, we will use this approach to study the spatiotemporal heterogeneity of *b* values

91   for the 2019 Changning M_S 6.0 earthquake.

92   The OK1993 model uses the seismic detection rate function $q(M)$ to describe the complete detection

93   degree of earthquake events with different magnitudes in the magnitude-frequency distribution:

94    $$q(M|\mu,\sigma) = \frac{1}{\sqrt{2\pi\sigma^2}} \int_{-\infty}^{M} e^{-\frac{(x-\mu)^2}{2\sigma^2}} dx \tag{1}$$

95   where M is the magnitude, the parameter μ represents the corresponding magnitude to the detection rate

96   of 50%, and σ indicates the corresponding magnitude range. The actual earthquake probability density

97   function and the log-likelihood function of the OK1993 model can be expressed as:

98    $$P(M|\beta,\mu,\sigma) = \frac{e^{-\beta M}q(M|\mu,\sigma)}{\int_{-\infty}^{+\infty} e^{-\beta M}q(M|\mu,\sigma)dM} = \beta e^{-\beta(M-\mu)+\beta^2\sigma^2/2} q(M|\mu,\sigma) \tag{2}$$

99    $$\ln L(\theta) = n\ln\beta - \sum_{i=1}^{n}[\beta M_i - \ln q(M_i|\mu,\sigma)] + n\beta\mu - \frac{n}{2}\beta^2\sigma^2 \tag{3}$$

100   The $\{M_1, M_2, \ldots, M_n\}$ in the above formula is the magnitude of a given series of observational events and

101   the power exponent $\beta = b\ln 10$, The parameter $[\beta, \mu, \sigma]$ can be obtained by fitting the above formula

102   using the maximum likelihood method. The Bayesian information criterion $BIC = -\ln L(\theta) +$

103   $k/2\ln(n)$ be adopted to calculate the corresponding BIC value and select the optimal models. Since

104   each grid node is composed of spatial coordinates $[x, y]$ and three parameters $[\beta, \mu, \sigma]$ in the OK1993

105   model, so the total number of freedom degrees is $k = 5 \times$ num of node in the entire study region.

106   The construction of the data-driven approach can be achieved by the Voronoi tessellation with limited

107   boundaries. Voronoi tessellation refer to a unique set of continuous polygon partitioning schemes $\{P_i, i$

108   $= 1, 2, \ldots, n\}$ given by a set of spatial nodes $S=\{s_1, s_2, \ldots, s_n\}$ in two-dimensional or three-dimensional

109   space. The polygon $P_i = \{x \mid \text{dist}(x, s_i) <= \text{dist}(x, s_j), i \neq j\}$, where $\text{dist}(a, b)$ denotes the Euclidean distance

110   between two points. Voronoi tessellation also benefits from the uniqueness of its spatial division, so it is

111   widely used in computing science, political elections, and many other studies (Rubner et al., 2000; Svec

112   et al*.,* 2007). The calculation steps of the data-driven approach include: (1) randomly throwing a certain

113   number of nodes in the study area and performing Voronoi meshing, with the number of grid nodes

114   gradually increasing from 2 to 40. To ensure that the Voronoi tessellation covers the possibility of various

115   spatial region segmentation, each number of grid nodes is randomly thrown 100 times. (2) Calculate

116   OK1993 model parameters and BIC values for $(2 + 3 + \ldots 40) \times 100 = 81900$ Voronoi cells obtained from

117   3900 tessellations (or spatial calculation models). Sum the BIC values of all the Voronoi cells obtained

118 from each tessellation and use it as the basis for judging whether this spatial calculation model is the

119 optimal model; (3) Among the 3900 spatial calculation models, 100 models (marked as best-100) with

120 smaller BIC values were selected as the optimal models, and the parameters $[\beta, \mu, \sigma]$ of the ensemble

121 median (Q_2) and median absolute deviation (MAD) were used as the final calculation results. The b value

122 can be obtained by $b = \beta / \ln 10$.

123 The maximum likelihood calculation of the OK1993 model parameter is not performed for the number

124 of earthquakes $N_1 < 5$ contained in a Voronoi cell, so the actual number of effective cells N_v obtained by

125 each tessellation is used, to distinguish the number of randomly thrown nodes. Although the value of N_1

126 may affect the parameter fitting error in some polygons with a small number of events, considering that

127 the OK1993 model in the form of continuous distribution function has the advantage of obvious fit

128 adaptability compared to the traditional linear Frequency-Magnitude Distribution (FMD) function in a

129 small number of data cases, this setting also ensures that the spatial division can obtain more polygon

130 calculation results, and the final result of the parameters is expressed by the ensemble median value, so

131 the effect of this method of value-taking on the final result is minimal.

132 In the above calculation steps, the setting of the maximum number of nodes, the number of random

133 throws, etc. has obvious subjectivity. However, due to the fact that the data-driven approach actually

134 obtains a very stable final result when the number of divisions and the number of grid nodes are sufficient

135 (Si and Jiang, 2019), for example, when the maximum number of nodes is 100, each type of nodes are

136 randomly thrown 1000 times, and the final result obtained when 1000 optimal models are selected is

137 almost the same as the result of this paper.

138 **Study Region and Data Used**

139 The 2019 Changning M_S 6.0 earthquake sequence occurred in the basin-mountain junction in the southern

140 margin of the Sichuan Basin, where the tectonic activity is relatively weak. The seismicity in the area is

141 mainly controlled by folds and associated faults. The intensity of historically destructive earthquakes is

142 low in the area where aftershocks extend. No earthquake with magnitude above 5.0 has been recorded in

143 this area before the Changning M_S 6.0 earthquake. According to Yi et al. (2019), it is inferred that the

144 occurrence of the Changning M_S 6.0 earthquake sequence may be related to the Baixiangyan-Shizitan

145 anticline and the Shuanghechang anticline and their associated fault activities. Figure 1 shows the study

146 area of this paper. We will focus on the rectangular area A'B'C'D' where the aftershock sequence mainly

147 occurred and the rectangular area ABCD where the surrounding earthquakes are active.

148 We used earthquake catalogs and bulletins provided by the Sichuan Regional Seismic Network from

149 2009/01/01 to 2019/07/17. To obtain relatively reliable parameters such as the epicenter location and

150 focal depth, the double-difference algorithm HypoDD (Waldhauser and Ellsworth, 2000) was used to

151 relocate the earthquakes. Among the data we used, a total of 21246 seismic events that meet the

152 requirements of the HypoDD method are not less than 4 arrivals, including 516649 P-wave arrivals,

153 506809 S-wave arrivals, and 59 permanent seismic stations and temporary seismic stations are used

154 which are located in Sichuan and surrounding provinces. We used a 12-layer one-dimensional crustal

155 velocity model (Xie et al., 2012) during the relocation. The ratio of V_P to V_S is set to 1.730.

156 A total of 18371 earthquake events were relocated (Fig. 1), of which the smallest event had a magnitude

157 of -1.0. Among them, 13728 and 4642 earthquakes before and after the M_S 6.0 mainshock, respectively.

158 The horizontal and vertical uncertainties are 0.425 km, 0.457 km and 0.654 km, respectively. The average

159 root mean square (RMS) of the travel-time residuals was reduced to 0.162 s. There were 2875 events

160 were discarded, which accounted for 13.53% of original catalogue. Most of their magnitudes range

161 between M_L 0.3 to M_L 1.4 (corresponding to the intervals of cumulative number 10% ~ 90%). Considering

162 that the data-driven approach used in this paper is the selection and ensemble averaging of a large number

163 of random space partitioning schemes, and that the OK1993 model is a continuous function of the

164 magnitude-frequency distribution, the effect of these excluded events on the calculation result of b value

165 can be ignored.

166 From the spatial distribution of the relocated earthquakes shown in Figure 1, the aftershocks are mainly

167 distributed in the northwest direction of the mainshock epicenter and extend along the Changning

168 anticline with a length about 27 km, which is much longer than the rupture scale of about 10 km for a M

169 6 earthquake accordance with the empirical formula given by Well and Coppersmith (1994). Besides,

170 the shape of the aftershock distribution is not simply linear; there are obvious inflections in the middle

171 segment, and in the northwest there is a branch approximately perpendicular to the direction of aftershock

172 distribution. There are relatively few aftershocks near the epicenter of the mainshock, and a large number

173 of aftershocks occurred in the northwest.

174 In the aftershock sequence of the Changning M_S 6.0 earthquake, there are 4 aftershocks with magnitudes

175 exceeding M_S 5.0, which are 2019/06/17 M_S 5.1, 2019/06/18 M_S 5.3, 2019/06/22 M_S 5.4, and 2019/07/04

176 M_S 5.6 earthquake, respectively.

177

178   Fig. 1

179 To facilitate the calculation of *b* values and the display of the results, we have selected only the events

180 within the rectangular area A'B'C'D' where almost all aftershocks are concentrated and the rectangular

181 area ABCD where a large number of earthquakes existed before the mainshock occurred. The positions

182 of these earthquakes were transformed by Cartesian coordinates and rotated according to the origin point

183 (104.986°E, 28.395°N) of the coordinates so that the aftershock sequence can be spread horizontally in

184 the new coordinate system. The epicenter distribution after coordinate transformation in Figure 2a-c

185 shows the spatiotemporal distribution on the distance versus rank of index 2-D map of the earthquake

186 within the rectangular frame A'B'C'D'.

187

188   Fig. 2

189 **Spatial Distributions of *b* Values on Surface and Depth Profiles**

190 According to the technical process of the data-driven approach described above, after Voronoi

191 tessellation, calculation of the BIC values, and selection of the optimal models, the ensemble median (Q_2)

192 and ensemble median absolute deviation (MAD) of *b* values can be obtained. Figure 3 shows an example

193 of calculating the parameters of the OK1993 model in terms of the frequency-magnitude distribution

194 based on a data-driven approach. Figure 3a is the distribution of those BIC values corresponding to the

195 number of effective cells N_V, and the red dots are the selected best-100 models. Figure 3b shows an

196 example in the best-100 models, that is, in the case of $N_V = 20$, the Voronoi tessellation in the rectangular

197 study area ABCD and the distribution of *b* values obtained by its calculation. Figure 3c shows an example

198 of the fitting result of the Ogata-Katsura 1993 model corresponding to a cell in Figure 3b. The OK1993

199 model parameters obtained by the fitting are $b = 0.714$, $\mu = 0.376$ and $\sigma = 0.247$.

200

201   Fig. 3

202 We calculated the distribution of the ensemble median *b* value in the rectangular region ABCD and the

203 depth profile of the rectangular region A'B'C'D', respectively. The results are shown in Figure 4. Figures

4a-b are the results before the Changning M_S6.0 earthquake and the entire study period, respectively. The results show that the b values exhibit a strong heterogeneous spatial distribution in the rectangular region ABCD before the Changning M_S6.0 earthquake. Low b values are mainly distributed in the eastern half of the area, with its lowest value being $b = 0.732$ and located near the epicenter of the mainshock. Low b value contours are mainly distributed in the NE-SW direction and are consistent with the direction of Shuanghechang anticline and their associated faults passing through the main epicenter. In the western part of the rectangular region ABCD, high b values are distributed, with a largest value of $b = 2.200$. This indicates that before the Changning M_S 6.0 earthquake, the differential stress near the epicenter of the mainshock was high, but the spatial scale of this larger differential stress was much smaller than the scale of the aftershock spatial distribution. The spatial distribution of b values calculated using all seismic events (see Fig. 4b) shows that the area with low b values in the region ABCD is significantly enlarged, and the b values in the rectangular region A'B'C'D' are almost less than 1.0 and further reduced to 0.698 near the epicenter of the mainshock. This phenomenon of a significant decrease in b value of the aftershock sequence after the mainshock widely exists in many earthquake cases (El-Isaa and Eatonb, 2014; Gulia and Wiemer, 2019).

Figures 4c-d show the distribution of ensemble median b value on the depth profile of the rectangular area A'B'C'D', and correspond to the results before the Changning M_S6.0 earthquake and all study periods, respectively. The calculation results after considering the depth information of the earthquake show that b values also have strong heterogeneity at different depths. Among them, in Figure 4c, low b values are mainly distributed at depth of 4 ~ 15 km and contains the source of the Changning M_S 6.0 earthquake and the 2019/06/17 M_S 5.1 earthquake. The lowest b value is about 0.493, which is much smaller than the minimum value in Figure 4a. In Figure 4d, considering the occurrence of the Changning M_S6.0 earthquake sequence, the distribution area of low b values expands in the NW direction, and the lowest b value is about 0.501, which is close to that in Figure 4c. Compared with the results obtained by ignoring the depth information of the earthquake in Figure 4a-b, the results obtained by Figure 4c-d reveal more significant heterogeneity of b values. When investigating this problem to the depth of the crust. Lower b values may indicate that there should be greater differential stress at the depth where the source area of the mainshock is located, and it is easily ignored by b value calculations that usually do not consider the depth information of earthquake events.

233

234   Fig. 4

235   Figure 5 shows the spatial distribution of the median absolute deviation (MAD) of b values by the data-

236   driven approach according to Figure 4. The ensemble MAD b value is smaller in the most region of

237   Figure 5a-d, especially in the rectangular region A'B'C'D', which implies that these regions have

238   relatively stable distribution and reliable ensemble median b values. As a comparison with Figures 4 and

239   Figure 5, we also used the Changning $M_S6.0$ earthquake and aftershocks to calculate the ensemble MAD

240   b values and the ensemble MAD b values. For the corresponding results, please see Figure S2 in the

241   *Supplementary Materials*.

242

243   Fig. 5

244   **Spatiotemporal Heterogeneity of b values**

245   Considering that b value usually changes over time before and after a strong earthquake, this paper not

246   only examines the spatial distribution of b values in the surface and depth profiles but also discusses the

247   spatiotemporal distribution of b values for earthquake events in the rectangular area A'B'C'D' where the

248   Changning $M_S 6.0$ sequence is located. Due to the strong temporal and spatial inhomogeneity of seismic

249   activity, especially clustering in time, this brings great difficulties to obtaining a stable and reliable b

250   value and clearly showing the temporal and spatial variation of the b value. In order to reduce this

251   difficulty to a certain extent, here we use the index of earthquake occurrence instead of time, that is, the

252   earthquake is projected on a pseudo-time axis of the index number of the occurrence time sequence.

253   Using the same calculation method as in Figure 4 and Figure 5, the distributions of ensemble median b

254   values and ensemble MAD b values on the distance-index map are obtained. The corresponding results

255   are shown in Figure 6 and Figure 7. Considering the possible abrupt change of the regional stress field

256   due to strong earthquakes such as the Changning $M_S6.0$ earthquake, we adopt two schemes to study the

257   spatiotemporal distribution of b values. One is to study the seismicity before and after the mainshock as

258   a whole, and the other is to study the seismicity before and after the mainshock as two independent

259   periods. The calculation results under the two schemes are shown in Figure 6a-b, respectively.

Fig. 6

It can be seen in Figure 6a that before the Changning M_S 6.0 earthquake, in the segment between -5 km and -10 km near the A'/B' end and a length of about 10 km (NW direction of the aftershocks in Fig. 1), showed relatively stable high b values, with the maximum value exceeding 2.0. In the segment between -5 km and 12 km near the C'/D' end and a length of about 17 km (the SE direction of the aftershocks in Figure 1, including the nucleation point of the mainshock), showed relatively stable low values before the Changning M_S 6.0 earthquake, and the range of the low b values gradually narrowed down and concentrated towards the nucleation point of the mainshock. After the Changning M_S 6.0 earthquake occurred, the b values in the entire spatial range from A'/B' to C'/D' decreased significantly. Among them, the b values in the 0 km ~ 12 km segment where the nucleation point of the mainshock is located have recovered rapidly, while the b values in the 0 km ~ -15 km segment have increased at a slower rate.

From the results before and after the Changning M_S 6.0 earthquake shown in Figure 6b, it can be seen that the occurrence of the mainshock has a greater impact on the continuity of time variant b values. This means that the spatiotemporal evolution image of the b values given in Figure 6a over the entire study period is not physically valid. Correspondingly, the decrease of pre-mainshock b values and the sudden expansion of the low b values may be a kind of artifact caused by the subsequent aftershocks brought into the calculation (Lei et al., 2019).

Compared with Figure 6a, the results in Figure 6b show that before the Changning M_S6.0 earthquake, the shortening and concentration changes for the low b value segment near the C'/D' end, and the expansion process of the high b value segment on the near the A'/B' end is performed simultaneously. This implies that a significantly higher differential stress area is concentrated toward the nucleation point of the mainshock. Figure 7 a-b show the distribution of ensemble MAD b values according to Figure 6 a-b, where higher ensemble MAD b values mainly appear in some areas with higher b values in Figure 6 a-b.
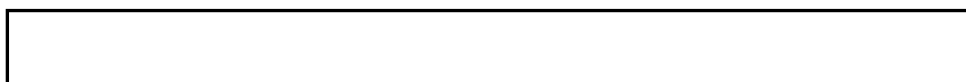
Fig. 7

Discussion

In the pattern of b value spatial heterogeneity before strong earthquakes, the locations of rupture nucleation points, sliding distributions, and aftershock distributions of some strong earthquakes were observed to correspond to areas with lower b values, such as the Parkfield $M = 6.0$ earthquake on September 28, 2004 (Wiemer and Wyss, 1997; Schorlemmer et al., 2004; Schorlemmer and Wiemer, 2005). However, the significant spatial heterogeneity of b values obtained from the studies of these earthquakes is suspected to be related to the subjective arbitrariness of the calculation rules (Kamer and Hiemer, 2015). The calculation results based on the data-driven method (Si and Jiang, 2019) in this paper show that significant spatial heterogeneity of b values can still be observed before the Changning $M_S6.0$ earthquake, especially on the depth profile of the fault. Moreover, according to the empirical relationship between the magnitude and rupture scale of Wells and Coppersmith (1994), the low-value spatial scale of $b < 0.75$ in Figure 4c is also close to the rupture length of about 10 km for the M 6.0 mainshock. This also means that it is still feasible to use the spatial heterogeneity of the b values to identify the locked asperities and determine the location of future strong earthquakes if more cases are verified.

There is still much controversy over the temporal variation pattern of b values in the source area before a strong earthquake. Although the decrease of b values prior to failure was found in laboratory fracturing experiments on relatively complete rock samples (e.g., Thompson et al., 2006; Lei, 2019) and the case study of strong earthquakes (Nanjo et al., 2012; Schurr et al., 2014; Bayrak et al., 2017; Huang et al., 2020), but a large number of reported temporal variations of b values before actual strong earthquakes are still considered to have no statistically significant predictive power (Parsons, 2007). Some studies have found that the temporal variation of b values corresponding to asperities are synchronized with loading rate and shear stress (Tormann et al., 2013). Schorlemmer et al. (2004) and Wiemer and Wyss (2002) studied some earthquake cases and concluded that the b value is quite stable over time and it is difficult to observe a significant change. The study of the relationship between acoustic emission events and stress in the stick-slip experiment shows that the complexity of the temporal variations of b values observed when sliding on rough fault planes may be due to fault-structure heterogeneity (Goebel et al., 2013). In this study of the Changning M_S 6.0 earthquake, we did not simply examine the temporal variations of b values in a fixed spatial range, but investigated the migration pattern of the b value in a 2-D spatiotemporal dimension. We found that as the time approaches the occurrence of the mainshock,

316   the spatial range of the low b values gradually shrinks and focuses on the vicinity of the rupture nucleation

317   point, and the b values does not decrease significantly. Under the assumption that the fault-structural

318   heterogeneity will not change in the short term, and based on previous understandings of the correlation

319   between high b values and fluid-induced seismicity, the migration pattern in this paper may be explained

320   by the erosion of fluid in the high differential stress area where the nucleation point is located.

321   For the spatiotemporal heterogeneity of the b value of the aftershocks of the 2019 Changning M_S 6.0

322   earthquake, we noticed that the aftershocks expanded spatially to areas with high pre-mainshock b values

323   in the northwest direction, and the length of the aftershock area was significantly longer than the rupture

324   scale of the earthquake (see Fig. 6b). Since the aftershocks do not exhibit relatively slow spatiotemporal

325   migration behavior, the physical mechanism that drives the aftershocks of this earthquake cannot be

326   explained by either the traditional stress corrosion model (Das and Scholz, 1981), or by frictional afterslip

327   model (Perfettini et al., 2018; Koper et al., 2018). Some views suggest that aftershock activity in high b

328   value regions may be related to the reactivation of highly fractured fault zones, the redistribution of stress

329   fields, and the role of fluids trapped in microfractures (Aktar et al., 2004). Long et al. (2020) imaging the

330   velocity structure of the area where the Changning M_S 6.0 earthquake was located, showing that there is

331   an obvious S-wave low-velocity anomaly at the depth of 3 to 8 km in the northwestern segment of the

332   aftershock. In this paper, this S-wave low-velocity anomaly region also corresponds to the distribution

333   of high b values, which may be related to the fluid intrusion. Therefore, we deduce that the abundant

334   aftershocks produced by this mainshock, and the active area that exceeds the rupture scale of the

335   mainshock are more likely to be caused by the mainshock which triggered a series of complex structural

336   aftershocks northwest of the nucleation point. The dynamic expansion of the high pre-mainshock b value

337   region to the nucleation point also creates conditions for the triggering of a large number of aftershocks

338   and the widespread spatially.

339   In addition, b values of the aftershocks first dropped rapidly to about 0.5, then gradually recovered, and

340   returned to the pre-seismic level after the fourth magnitude 5 strong aftershock (excluding high b value

341   areas). The phenomenon that the b values of the aftershock sequence decreases immediately after the

342   mainshock to a rapid recovery has been observed in many earthquake cases (El-Isaa and Eatonb, 2014;

343   Tormann et al., 2015). Unlike most aftershock sequences, where the b value generally increases by 20%

344   after the mainshock, this sudden decrease in b value is considered to be related to the occurrence of

345   subsequent strong aftershocks or larger earthquakes (Gulia and Wiemer, 2019). In the aftershock

346 sequence of the Changning M_S6.0 earthquake, the rapidly decreasing b value of the aftershocks was

347 accompanied by 4 strong aftershocks with magnitudes greater than 5.0, which is consistent with the

348 phenomenon revealed by previous studies. This may also support the idea of discrimination between

349 foreshocks and aftershocks by real-time monitoring of the b value in aftershock sequences (Gulia and

350 Wiemer, 2019). However, it needs to be pointed out that similar to the problem of sudden changes in the

351 spatiotemporal distribution of b values before and after the main shock, it cannot rule out that 4 strong

352 aftershocks with M>5 will affect the continuity of the b values to a certain extent.

Conclusions

354 To reveal whether there is spatiotemporal heterogeneity of b values before and after the 2019 Changning

355 M_S 6.0 earthquake, and to overcome the subjectivity of the choice of data used for calculation, we applied

356 the OK1993 model of magnitude-frequency distribution according to the data-driven idea to calculate b

357 values. We also investigated the distribution characteristics of b values from three different ways:

358 horizontal surface distribution, depth profile distribution, and in the distance-rank of index map. The

359 main conclusions are as follows:

360 1. The b values before and after the Changning M_S 6.0 earthquake showed strong spatiotemporal

361 heterogeneity on the horizontal surface distribution, depth profile distribution, and distance-rank of index

362 map. Among them, before the Changning M_S 6.0 earthquake, there were obvious low b value distributions

363 near the epicenter of the mainshock and within the depth range of 3 to 12 km. The correlation shows that

364 there may be significantly higher differential stress in the source area before the Changning M_S 6.0

365 earthquake. The northwestern segment of the aftershocks has a distinctly high b value distribution, which

366 coincides with the S-wave low-velocity anomaly region shown by the velocity structure imaging.

367 2. The b value spatiotemporal distribution results show that before the Changning M_S 6.0 earthquake, the

368 high b value region of the NW segment spread by aftershocks gradually expanded and approached the

369 nucleation point as the time approached the failure time of mainshock. This may be related to the fluid

370 intrusion in the rock. A large number of aftershocks were produced and the area where the aftershocks

371 were spread was significantly larger than the rupture scale of the mainshock. The mainshock may

372 triggered seismicity in the NW direction where the fluid intrudes.

373 3. The b values of the aftershocks of the Changning M_S 6.0 earthquake decreased rapidly and gradually

374 recovered after the mainshock, indicating a higher differential stress level in the aftershock area. The

375 time variation of low b value is synchronized with the occurrence of strong aftershocks with M $\geq$ 5.0,

376 showing the application potential that can be used to distinguish between foreshocks and aftershocks.

377 4. Although the distribution characteristics of b values before and after the Changning M_S 6.0 earthquake

378 were qualitatively consistent when they were studied in different space-time dimensions, there were

379 significant differences in specific b value. For example, the minimum b value of the Changning M_S 6.0

380 earthquake on the depth profile distribution is about 0.493, but it is about 0.732 when the seismic depth

381 information is ignored and only calculated on the surface. This inconsistency needs special attention

382 when studying the spatiotemporal heterogeneity of b values.

383 **Acknowledgment**

384 This study is supported by the program of China Seismic Experimental Site (CSES, No. 2019CSES0106),

385 the program of basic resources investigation of science and technology (No. 2018FY100504), the

386 National Natural Science Foundation of China (No. U2039204), and the Special Fund of the Institute of

387 Geophysics, China Earthquake Administration (No.DQJB20X11). The earthquake catalog used in this

388 paper was provided by the Sichuan Earthquake Agency. The Multi-Parametric Toolbox 3.0

389 (https://www.mpt3.org/Main/HomePage, last accessed June 2018) is used for the analysis of parametric

390 optimization and computational geometry. We thank the editor and two anonymous reviewers for their

391 very helpful comments and suggestions.

392 **References**

393 Aktar, M., S. Özalaybey, M. Ergin, H. Karabulut, M.-P. Bouin, C. Tapırdamaz, F. Biçmen, A. Yörük

394 and M. Bouchon (2004). "Spatial variation of aftershock activity across the rupture zone of the 17

395 August 1999 Izmit earthquake, Turkey." Tectonophysics **391**(1-4): 325-334.

396 Amelung, F. and G. King (1997). "Earthquake scaling laws for creeping and non-creeping faults."

397 Geophysical Research Letters **24**(5): 507-510.

398 Amorèse, D., J.-R. Grasso and P. Rydelek (2010). "On varying b-values with depth: results from

399 computer-intensive tests for Southern California." Geophysical Journal International **180**(1): 347-

400 360.

401 Bayrak, E., S. Yılmaz and Y. Bayrak (2017). "Temporal and spatial variations of Gutenberg-Richter
402 parameter and fractal dimension in Western Anatolia, Turkey." Journal of Asian Earth Sciences,
403 **138**: 1-11.

404 Das, S. and C. Scholz (1981). "Theory of time-dependent rupture in the Earth." Journal of
405 Geophysical Research: Solid Earth **86**(B7): 6039-6051.

406 Del Pezzo, E., F. Bianco and G. Saccorotti (2003). "Duration magnitude uncertainty due to seismic
407 noise: Inferences on the temporal pattern of GR *b*-value at Mt. Vesuvius, Italy." Bulletin of the
408 Seismological Society of America **93**(4): 1847-1853.

409 El-Isaa, Z. H. and D. W. Eatonb (2014). "Spatiotemporal variations in the b-value of earthquake
410 magnitude–frequency distributions: Classification and causes. " Tectonophysics **615–616**: 1-11.

411 Goebel, T. H. W., D. Schorlemmer, T. Becker, G. Dresen and C. Sammis (2013). "Acoustic
412 emissions document stress changes over many seismic cycles in stick-slip experiments."
413 Geophysical Research Letters **40**(10): 2049-2054.

414 Gulia, L. and S. Wiemer (2019). "Real-time discrimination of earthquake foreshocks and
415 aftershocks." Nature **574**(7777): 193-199.

416 Gulia, L., S. Wiemer and D. Schorlemmer (2010). "Asperity-based earthquake likelihood models
417 for Italy." Annals of Geophysics **53**(3): 63-75.

418 Hainzl, S. and T. Fischer (2002). "Indications for a successively triggered rupture growth underlying
419 the 2000 earthquake swarm in Vogtland/NW Bohemia." Journal of Geophysical Research: Solid
420 Earth **107**(B12): ESE 5-1-ESE 5-9.

421 Huang, H., L. S. Meng, R. Bürgmann, W. Wang and K. Wang (2020), "Spatio-temporal foreshock
422 evolution of the 2019 M 6.4 and M 7.1 Ridgecrest, California earthquakes." Earth and Planetary
423 Science Letters, **551**: 116582.

424 Hutton, K., J. Woessner and E. Hauksson (2010). "Earthquake monitoring in southern California
425 for seventy-seven years (1932–2008)." Bulletin of the Seismological Society of America **100**(2):
426 423-446.

427 Kagan, Y. Y. (1999). "Universality of the seismic moment-frequency relation." Pure and Applied
428 Geophysics **155**(2): 537-573.

429 Kamer, Y. and S. Hiemer (2015). "Data-driven spatial *b* value estimation with applications to
430 California seismicity: To *b* or not to *b*." Journal of Geophysical Research: Solid Earth **120**(7): 5191-
431 5214.

432 Koper, K. D., K. L. Pankow, J. C. Pechmann, J. M. Hale, R. Burlacu, W. L. Yeck, H. M. Benz, R.
433 B. Herrmann, D. T. Trugman and P. M. Shearer (2018). "Afterslip enhanced aftershock activity
434 during the 2017 earthquake sequence near Sulphur Peak, Idaho." Geophysical Research Letters
435 **45**(11): 5352-5361.

436 Lei, X. L. (2019). "Evolution of *b*-value and fractal dimension of acoustic emission events during
437 shear rupture of an immature fault in Granite." Applied Sciences **9**(12): 2498.

438 Lei, X. L. and T. Satoh (2007). "Indicators of critical point behavior prior to rock failure inferred
439 from pre-failure damage." Tectonophysics **431**(1-4): 97-111.

440 Lei, X., Z. Wang and J. Su (2019). "Possible link between long-term and short-term water injections
441 and earthquakes in salt mine and shale gas site in Changning, south Sichuan Basin, China." Earth
442 and Planetary Physics **3**(6): 510-525.

443 Long, F., Z. Zhang, Y. Qi, M. Liang, X. Ruan, W. Wu, G. Jiang and L. Zhou (2020). "Three
444 dimensional velocity structure and accurate earthquake location in Changning–Gongxian area of
445 southeast Sichuan." Earth and Planetary Physics **4**(2): 1-15.

446 Mori, J. and R. E. Abercrombie (1997). "Depth dependence of earthquake frequency-magnitude
447 distributions in California: Implications for rupture initiation." Journal of Geophysical Research:
448 Solid Earth **102**(B7): 15081-15090.

449 Murru, M., R. Console, G. Falcone, C. Montuori and T. Sgroi (2007). "Spatial mapping of the *b*
450 value at Mount Etna, Italy, using earthquake data recorded from 1999 to 2005." Journal of
451 Geophysical Research: Solid Earth **112**: B12303.

452 Nandan, S., G. Ouillon, S. Wiemer and D. Sornette (2017). "Objective estimation of spatially
453 variable parameters of epidemic type aftershock sequence model: Application to California."
454 Journal of Geophysical Research: Solid Earth **122**(7): 5118-5143.

455   Nanjo, K. Z., N. Hirata, K. Obara and K. Kasahara (2012). "Decade‐scale decrease in *b* value prior
456   to the M9‐class 2011 Tohoku and 2004 Sumatra quakes." Geophysical Research Letters **39**:
457   L20304.

458   Ogata, Y. (2011). "Significant improvements of the space-time ETAS model for forecasting of
459   accurate baseline seismicity." Earth, Planets and Space **63**(3): 6.

460   Ogata, Y. and K. Katsura (1993). "Analysis of temporal and spatial heterogeneity of magnitude
461   frequency distribution inferred from earthquake catalogues." Geophysical Journal International
462   **113**(3): 727-738.

463   Parsons, T. (2007). "Forecast experiment: Do temporal and spatial *b* value variations along the
464   Calaveras fault portend M $\geq$ 4.0 earthquakes?" Journal of Geophysical Research: Solid Earth
465   **112**(B3): B03308.

466   Perfettini, H., W. Frank, D. Marsan and M. Bouchon (2018). "A model of aftershock migration
467   driven by afterslip." Geophysical Research Letters **45**(5): 2283-2293.

468   Rubner, Y., C. Tomasi, L. J. Guibas (2000). "The earth mover's distance as a metric for image
469   retrieval. " International Journal of Computer Vision **40**: 99-121.

470   Sambridge, M., T. Bodin, K. Gallagher and H. Tkalčić (2013). "Transdimensional inference in the
471   geosciences." Philosophical Transactions of the Royal Society A: Mathematical, Physical and
472   Engineering Sciences **371**(1984): 20110547.

473   Scholz, C. H. (1968). "The frequency-magnitude relation of microfracturing in rock and its relation
474   to earthquakes." Bulletin of the seismological society of America **58**(1): 399-415.

475   Schorlemmer, D. and S. Wiemer (2005). "Microseismicity data forecast rupture area." Nature
476   **434**(7037): 1086-1086.

477   Schorlemmer, D., S. Wiemer and M. Wyss (2004). "Earthquake statistics at Parkfield: 1. Stationarity
478   of *b* values." Journal of Geophysical Research: Solid Earth **109**(B12).

479   Schurr B, G. Asch, S. Hainzl, J. Bedford, A. Hoechner, M. Palo, R. Wang, M. Moreno, M. Bartsch,
480   Y. Zhang, O. Oncken, F. Tilmann, T. Dahm, P. Victor, S. Barrientos and J. Vilotte (2014). "Gradual

481 unlocking of plate boundary controlled initiation of the 2014 Iquique earthquake." Nature **512**: 299-
482 302.

483 Si, Z. Y. and C. S. Jiang (2019). "Research on parameter calculation for the Ogata–Katsura 1993
484 model in terms of the frequency–magnitude distribution based on a data-driven approach."
485 Seismological Research Letters **90**(3): 1318-1329.

486 Stirling, M. W., S. G. Wesnousky and K. Shimazaki (1996). "Fault trace complexity, cumulative
487 slip, and the shape of the magnitude-frequency distribution for strike-slip faults: A global survey."
488 Geophysical Journal International **124**(3): 833-868.

489 Svec, L., S. Burden, A. Dilley (2007). "Applying Voronoi diagrams to the redistricting problem. "
490 The UMAP Journal **28**: 313-32.

491 Thompson, B. D., R. P. Young and D. A. Lockner (2006). "Fracture in Westerly granite under AE
492 feedback and constant strain rate loading: nucleation, quasi-static propagation, and the transition to
493 unstable fracture propagation." Pure and Applied Geophysics **163**(5-6): 995-1019.

494 Toda, S., R. S. Stein, P. A. Reasenberg, J. H. Dieterich and A. Yoshida (1998). "Stress transferred
495 by the 1995 M_w= 6.9 Kobe, Japan, shock: Effect on aftershocks and future earthquake probabilities."
496 Journal of Geophysical Research: Solid Earth **103**(B10): 24543-24565.

497 Tormann, T., B. Enescu, J. Woessner, and S. Wiemer (2015). "Randomness of megathrust
498 earthquakes implied by rapid stress recovery after the Japan earthquake." Nature Geoscience **8**: 152-
499 158.

500 Tormann, T., S. Wiemer, S. Metzger, A. Michael, and J. L. Hardebeck (2013). "Size distribution of
501 Parkfield's microearthquakes reflects changes in surface creep rate." Geophysical Journal
502 International **193**: 1474-1478.

503 Urbancic, T. I., C. I. Trifu, J. M. Long and R. P. Young (1992). "Space-time correlations of *b* values
504 with stress release." Pure and Applied Geophysics **139**(3-4): 449-462.

505 Waldhauser, F. and W. L. Ellsworth (2000). "A double-difference earthquake location algorithm:
506 method and application to the Northern Hayward fault, California." Bulletin of the Seismological
507 Society of America **90**(6): 1353-1368.

508 Wells, D. L. and K. J. Coppersmith (1994). "New empirical relationships among magnitude, rupture

509 length, rupture width, rupture area, and surface displacement." Bulletin of the seismological Society

510 of America **84**(4): 974-1002.

511 Wiemer, S. and D. Schorlemmer (2007). "ALM: An asperity-based likelihood model for

512 California." Seismological Research Letters **78**(1): 134-140.

513 Wiemer, S. and M. Wyss (1997). "Mapping the frequency-magnitude distribution in asperities: An

514 improved technique to calculate recurrence times?" Journal of Geophysical Research: Solid Earth

515 **102**(B7): 15115-15128.

516 Wiemer, S. and M. Wyss (2002). Mapping spatial variability of the frequency-magnitude

517 distribution of earthquakes. Advances in Geophysics **45:** 259-302.

518 Woessner, J. and S. Wiemer (2005). "Assessing the quality of earthquake catalogues: Estimating

519 the magnitude of completeness and its uncertainty." Bulletin of the Seismological Society of

520 America **95**(2): 684-698.

521 Wyss, M. (1973). "Towards a physical understanding of the earthquake frequency distribution."

522 Geophysical Journal of the Royal Astronomical Society **31**(4): 341-359.

523 Wyss, M., D. Schorlemmer and S. Wiemer (2000). "Mapping asperities by minima of local

524 recurrence time: San Jacinto-Elsinore fault zones." Journal of Geophysical Research: Solid Earth

525 **105**(B4): 7829-7844.

526 Xie, J., S. Ni and X. Zeng (2012). "1 D shear wave velocity structure of the shallow upper crust in

527 central Sichuan Basin." Earthquake Research in Sichuan (in Chinese) **143**(2): 20-24.

528 Yi, G. X., F. Long, M. J. Liang, M. Zhao, S. W. Wang, Y. Gong, H. Z. Qiao and J. R. Su (2019).

529 "Focal mechanism solutions and seismogenic structure of the 17 June 2019 M_S 6.0 Sichuan

530 Changning earthquake sequence." Chinese Journal of Geophysics (in Chinese) **62**(9): 3432-3447.

531

532

533

534
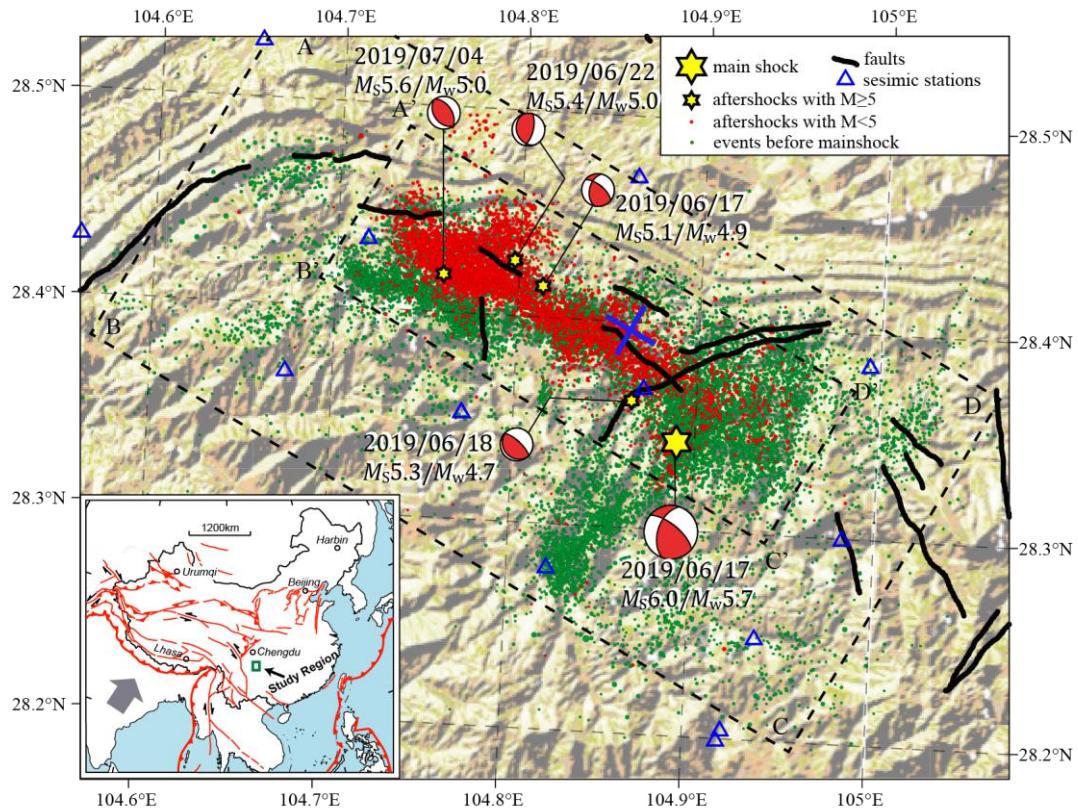
Fig. 1 Distribution of seismicity in the Changning area. The red dots show the aftershocks of the Changning M_S 6.0 earthquake, and the green dots indicate the earthquakes that occurred before the Changning M_S 6.0 earthquake. Hexagonal stars mark the position of the mainshock and four aftershocks with magnitude no less than 5.0, and the corresponding focal mechanisms are marked. The dotted rectangular ABCD and A'B'C'D' show the two spatial regions for calculating the b value and rotating the coordinate system, and the blue cross symbol gives the origin where the coordinate system is rotated. The blue triangles show the location of seismic stations that record these earthquakes, and the solid black lines represent active faults (He et al., 2019). The study region is shown in the location figure in the bottom-left by a green rectangle.
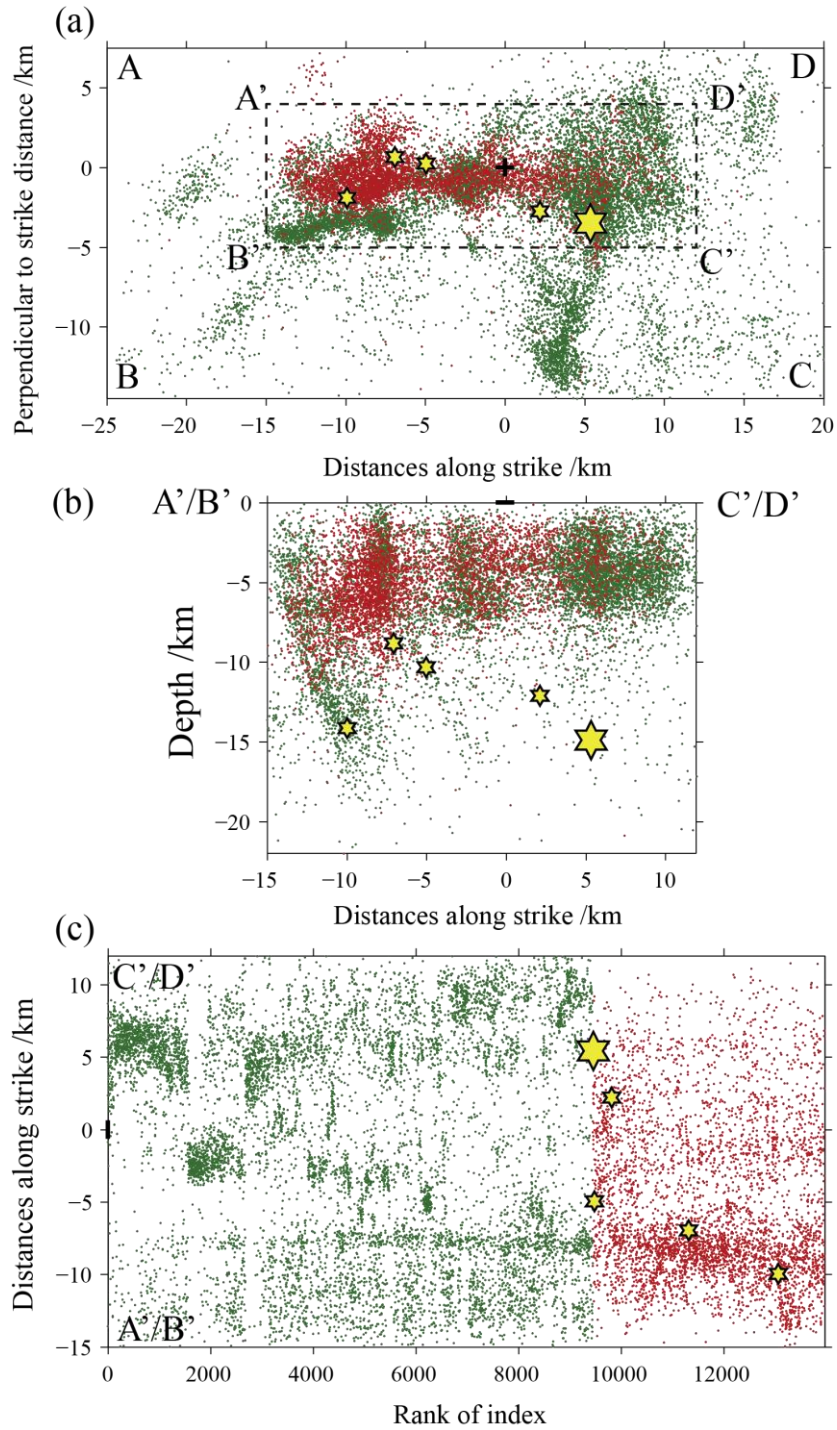
Fig. 2 Distribution of seismicity for *b* values calculations. (a) Rotating the coordinate system to the seismic distribution along the direction of the aftershock distribution; (b) Projecting the earthquakes in the rectangular frame A'B'C'D' on the depth profile; (c) The temporal and spatial distribution on the distance versus rank of index 2-D map of the earthquakes within the rectangular frame A'B'C'D'. The meaning of the symbols is the same as in Fig. 1.
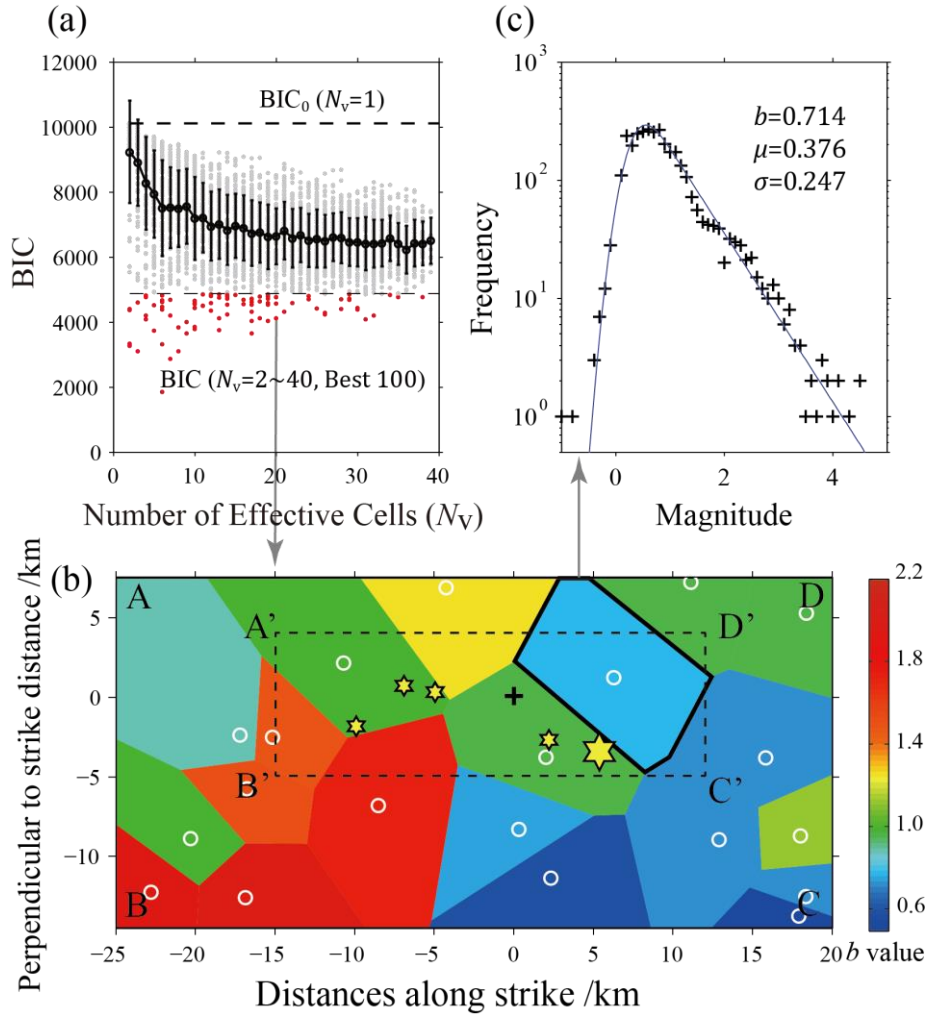
Fig. 3 An example of calculating the parameters of the Ogata-Katsura 1993 model in terms of the frequency-magnitude distribution based on a data-driven approach. (a) Distribution of BIC values versus the number of effective cells N_v in the Voronoi tessellation. The black dots and error bars are commensurate with the mean value and one standard deviation of BIC values under the corresponding N_v, respectively. The top horizontal dashed line marks the BIC values of the entire spatial region without mesh generation (BIC$_0$, N_v =1). The red dots show the BIC values with the best-100 solutions are selected, while the gray dots are the other BIC results according to N_v. (b) Example of Voronoi tessellation of N_v=20 and one of the best-100 models selected. The white circles are the positions of the Voronoi nodes, and the resulting partitions are color coded by their estimated b values (obtained from the β-value in the Ogata-Katsura 1993 model). (c) Example of fitting result for the frequency–magnitude distribution (FMD) of the Ogata–Katsura 1993 (OK1993) model in the Voronoi cell indicated by a thick line in subgraph (b).
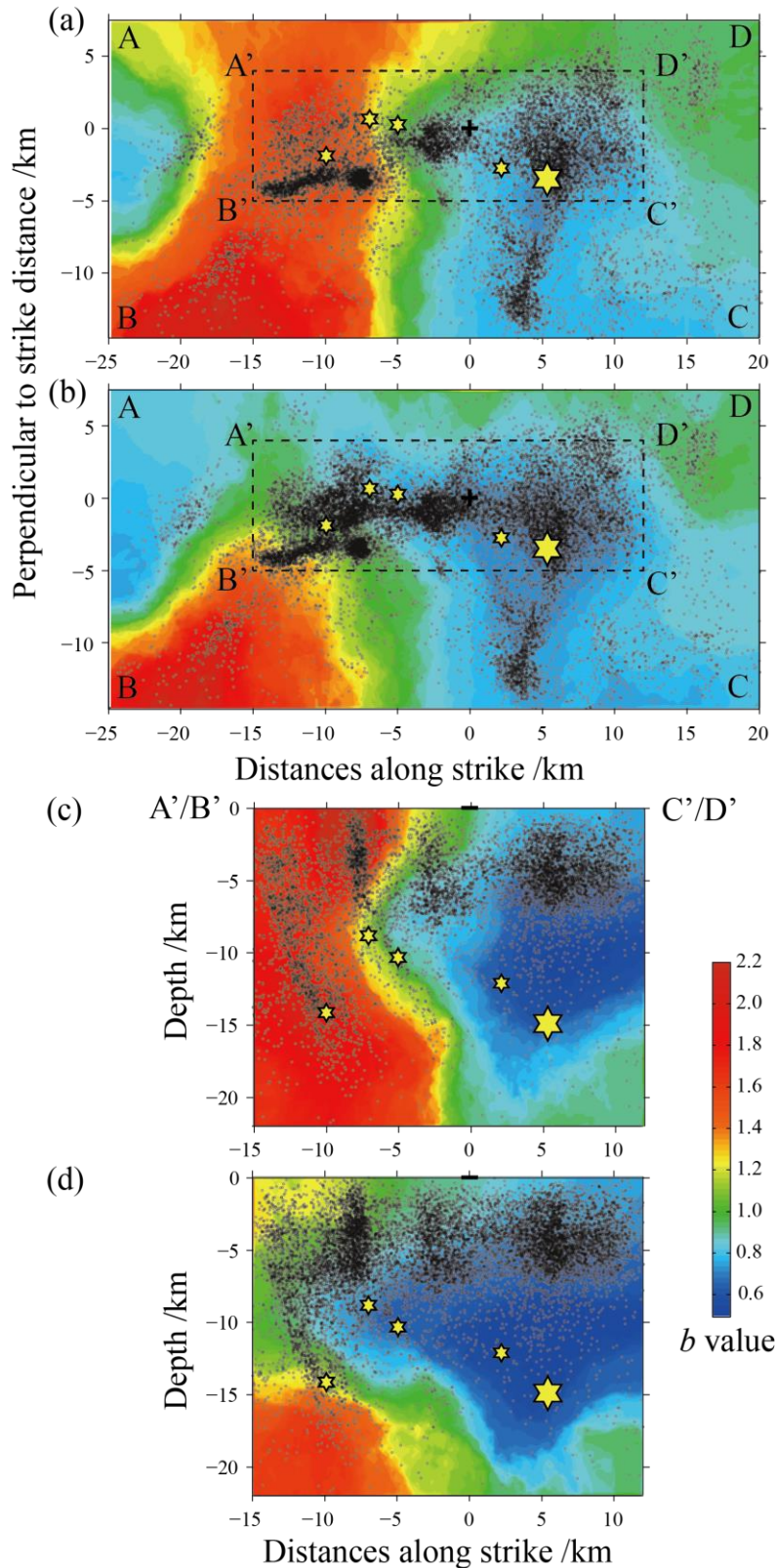
567   **Fig. 4 The spatial distribution of the ensemble median *b* values of the best-100 solutions for *N*ᵥ=2~40 in the**

568   **Changning area. (a) The ensemble median *b* values before the Changning *M*ₛ 6.0 earthquake is**

569   **distributed on the horizontal plane after the rotation; (b) The ensemble median *b* values obtained by**

570   **calculation of all the earthquake including the aftershocks of the Changning *M*ₛ 6.0 earthquake is**

571   **distributed on the horizontal plane after the rotation; (c) distribution of the ensemble median *b* values**

572   before the occurrence of the Changning M_S 6.0 earthquake in the rectangular frame A'B'C'D' on the

573   depth profile; (d) distribution of ensemble median b values obtained by calculation of all earthquakes

574   including aftershocks of the Changning M_S 6.0 earthquake in the rectangular frame A'B'C'D' on the

575   depth profile. The black dots on each subgraphs mark the seismic events used in the calculation.
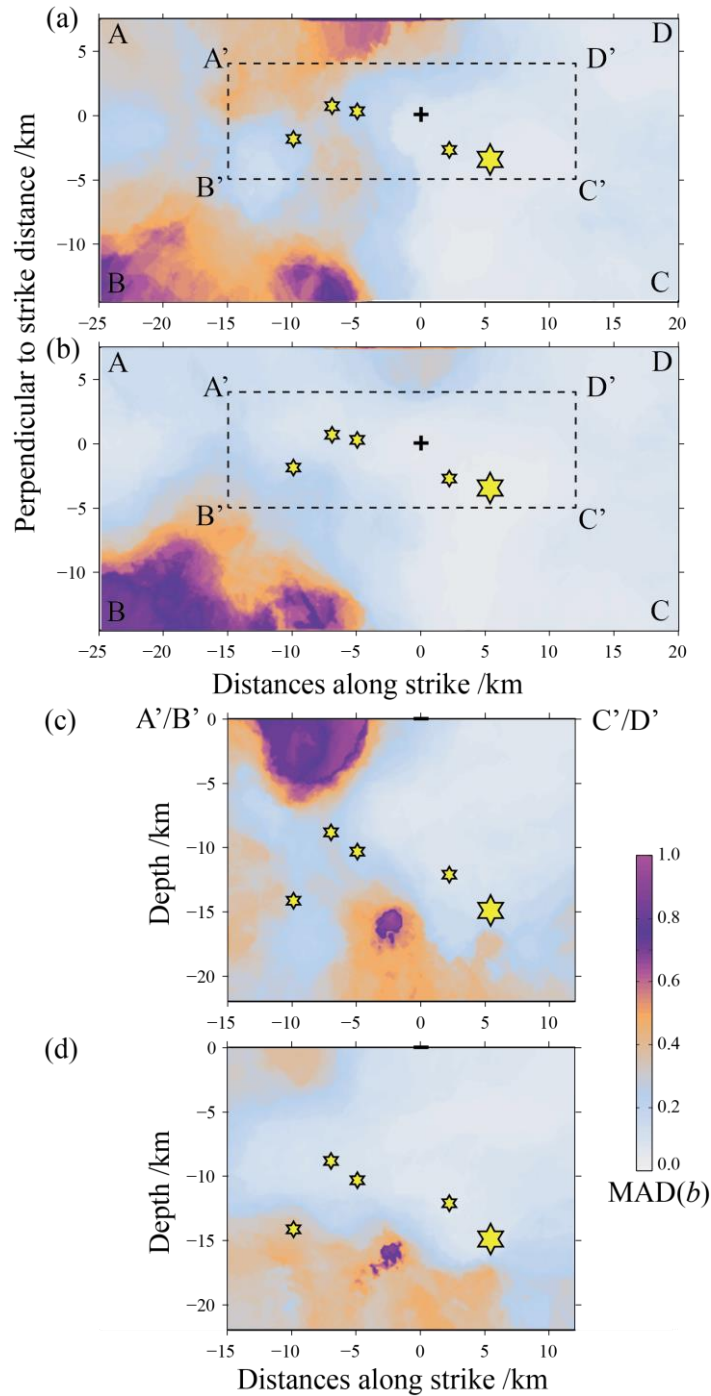
576

577 **Fig. 5 The spatial distribution of the median absolute deviation (MAD) of the *b* values by the data-driven**

578 **approach according to figure 4. (a) The ensemble MAD *b* values before the Changning *M*S 6.0**

579 **earthquake is distributed on the horizontal plane after the rotation; (b) The ensemble MAD *b* values**

580 **obtained by calculation of all the earthquake including the aftershocks of the Changning *M*S 6.0**

581 **earthquake is distributed on the horizontal plane after the rotation; (c) distribution of the ensemble**

582 **MAD *b* values before the occurrence of the Changning *M*S 6.0 earthquake in the rectangular frame**

583 **A'B'C'D' on the depth profile; (d) distribution of ensemble MAD *b* values obtained by calculation of**

584 **all earthquakes including aftershocks of the Changning *M*S 6.0 earthquake in the rectangular frame**

585 **A'B'C'D' on the depth profile.**
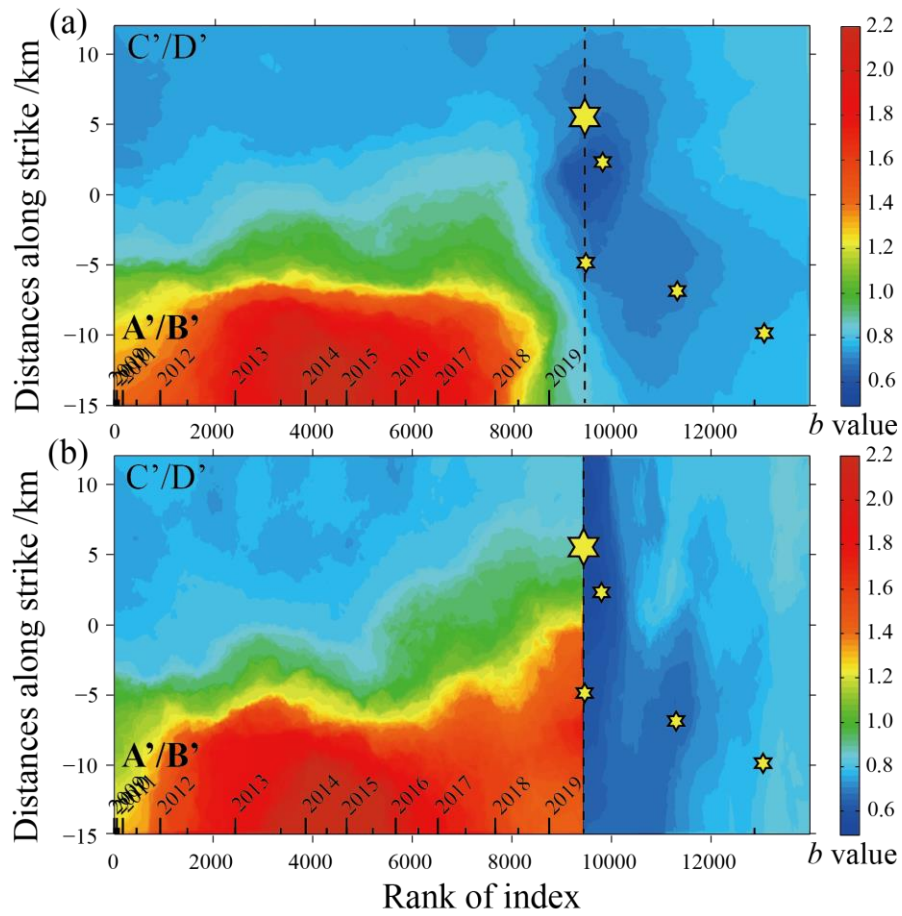
Fig. 6 Spatiotemporal distribution of the ensemble median *b* values of the best-100 solutions for N_v=2~40 on a 2-D space consisting of distance alone strike and rank of index. (a) The ensemble median *b* values obtained from all data before and after the Changning M_S 6.0 earthquake; (b) The ensemble median *b* values obtained from the data before and after the Changning M_S 6.0 earthquake, respectively. The vertical dotted line shows where the M_S 6.0 earthquake occurred. The time scale is marked at the upper *x*-axis, including the time of whole year marked by long tick and the half-year time marked by short tick.

595
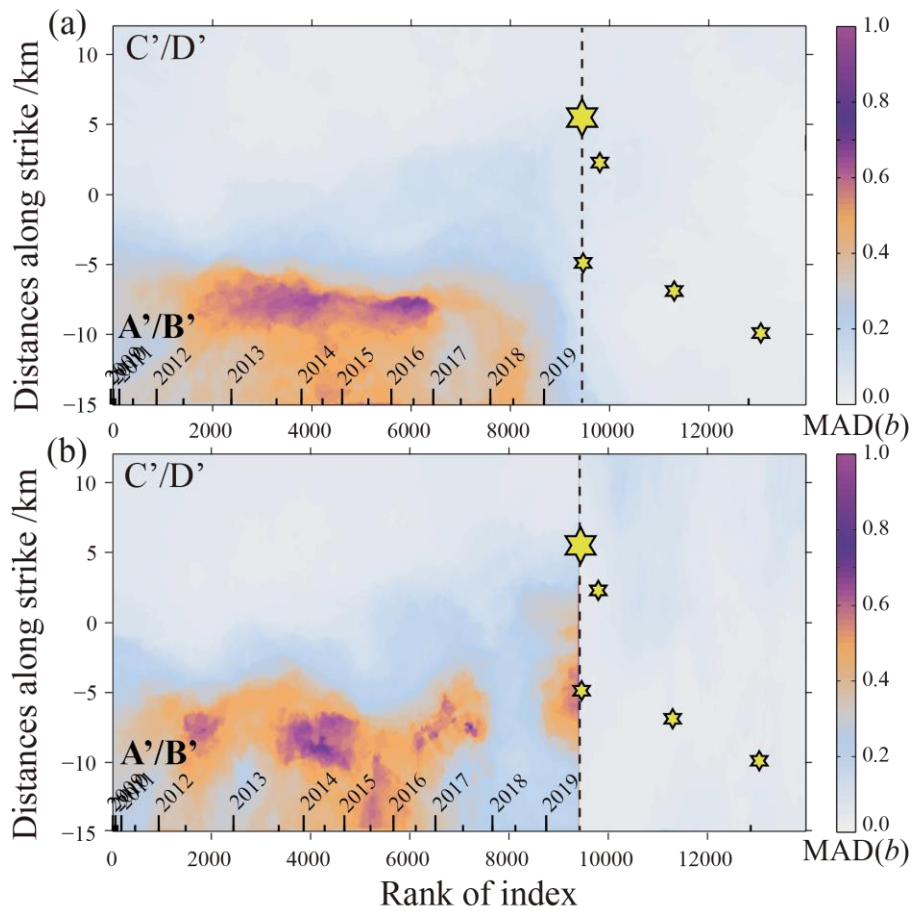
596

597 **Fig. 7 Spatiotemporal distribution of the median absolute deviation (MAD) of the *b* values of the best-100**

598   **solutions for *N*ᵥ=2~40 on a 2-D space consisting of distance alone strike and rank of index. (a) The**

599   **ensemble MAD *b* values obtained from all data before and after the Changning *M*ₛ 6.0 earthquake; (b)**

600   **The ensemble MAD *b* values obtained from the data before and after the Changning *M*ₛ 6.0 earthquake,**

601   **respectively. The vertical dotted line shows where the *M*ₛ 6.0 earthquake occurred. The time scale is**

602   **marked at the upper *x*-axis, including the time of whole year marked by long tick and the half-year**

603   **time marked by short tick.**